Materials Today Physics 20 (2021) 100444

Contents lists available at ScienceDirect

Materials Today Physics

journal homepage: https://www.journals.elsevier.com/materials-today-physics

Band structure and microstructure modulations enable high quality factor to elevate thermoelectric performance in $Ge_{0.9}Sb_{0.1}Te$-x%$FeTe_2$

Yang Jin [a, 1], Tao Hong [a, 1], Dongyang Wang [a], Yu Xiao [a], Wenke He [a], Xiang Gao [c], Yuting Qiu [b, **], Li-Dong Zhao [a, *]

[a] School of Materials Science and Engineering, Beihang University, Beijing 100191, China
[b] Beihang School, Beihang University, Beijing 100191, China
[c] Center for High Pressure Science and Technology Advanced Research (HPSTAR), Beijing 100094, China

HPSTAR 1151-2021

ARTICLE INFO

Article history:
Received 10 May 2021
Received in revised form
18 May 2021
Accepted 19 May 2021
Available online 9 June 2021

Keywords:
Thermoelectric
Quality factor
$FeTe_2$
Density of states
Lattice thermal conductivity

ABSTRACT

GeTe is an excellent mid-temperature thermoelectric material with various freedom degrees to tune the thermoelectric performance, which has drawn intensive attentions. Herein, superior thermoelectric performance of GeTe-based materials is achieved through significantly elevating quality factor B with $FeTe_2$ introduction. First-principles calculations show that introducing $FeTe_2$ into GeTe can increase the density of states due to the contribution of the 3d orbital of Fe, leading to an enhancement of effective mass from ~2.21m_0 in Fe-free sample to ~3.01 m_0 in $Ge_{0.9}Sb_{0.1}Te$−2%$FeTe_2$, which could maintain high electrical transport properties. Meanwhile, the lattice thermal conductivity is drastically suppressed by Van der Waals gaps, Fe-rich nanoprecipitates and strain field fluctuations with minimal disruption on carrier transport, leading to a minimum lattice thermal conductivity of ~0.54 Wm^{-1} K^{-1}. Ultimately, a superior ZT ~2.1 at 723 K and a ZT_{ave} of ~1.25 at 300−773 K are attained in $Ge_{0.9}Sb_{0.1}Te$−1%$FeTe_2$.

1. Introduction

Thermoelectricity has been widely recognized as an eco-friendly technology that can reversibly convert electricity into heat. The conversion efficiency can be elevated by the dimensionless figure of merit, $ZT = S^2\sigma T(\kappa_{ele}+\kappa_{lat})^{-1}$, where S represents Seebeck coefficient, σ denotes electrical conductivity, T represents absolute temperature, κ_{ele} represents electronic thermal conductivity, and κ_{lat} represents lattice thermal conductivity [1–5]. These parameters are strongly correlated with each other, such as the compromises between Seebeck coefficient and carrier concentration, effective mass and carrier mobility, carrier mobility and lattice thermal conductivity *et al.* [6] Although it is a big challenge to decouple these interdependent parameters, numerous endeavors are dedicated to optimizing thermoelectric (TE) performance [7,8]. Adjusting carrier concentration to an optimal range [9–12] and modulating band structure [13–17] are effective methods to balance electrical conductivity and Seebeck coefficient, which can lead to an optimum power factor ($PF = S^2\sigma$). Moreover, it has been reported that introducing transitional elements in TE materials has a positive effect on band structure modulation due to their d orbital electron [13,18–20]. Meanwhile, the lattice thermal conductivity, a phonon transport property, is relatively independent, which can be reduced through suppressing phonon propagation *via* manipulating microstructures [11,21–23]. Although defects affect both thermal and electrical transport properties, controlling nanoscale architectures in materials opens an avenue to scatter phonons rather than carriers due to their lengths with different scales [24–27].

Among TE materials in mid-temperature region, GeTe stands out due to its superior electrical transport property and is expected to be a substitute for PbTe without lead [28]. The existence of numerous Ge vacancies in pristine GeTe has a negative effect on TE performance. Thus, In [29], Sb [30–32], and Bi [9,17,33] are extensively employed to optimize carrier concentration. Meanwhile, GeTe as an analogue of lead telluride owns multiple bands, which provides a degree of freedom to promote electrical transport property through tuning band structure [14,16]. It has been reported that incorporating MnTe into GeTe manipulated the band structure, which was associated with the 3*d* orbital of the Mn

** Corresponding author.
* Corresponding author.
E-mail addresses: qyt2014@buaa.edu.cn (Y. Qiu), zhaolidong@buaa.edu.cn (L.-D. Zhao).
[1] Theses authors contributed equally to this work.

https://doi.org/10.1016/j.mtphys.2021.100444
2542-5293/

element [32]. Moreover, a rather high lattice thermal conductivity in pristine GeTe also limits the promotion of its thermal transport property. Entropy engineering [34], pseudo-layered structuring [21,35], phase separation [36,37], introducing nanoprecipitates [16,38], *etc*. have been successfully realized in GeTe systems for descending lattice thermal conductivity.

In our previous work, we adjusted carrier concentration to an optimum range in intrinsic GeTe by Sb counter-doping [39]. In this work, we investigated the TE performance of $Ge_{0.9}Sb_{0.1}Te$ with taking into account the 3*d* orbital of the Fe element through introducing $FeTe_2$, whose formation energy is the lowest among Fe_mTe_n [40]. And we expect to reduce lattice thermal conductivity through precipitating Fe-riched microstructures. Thus, we choose $FeTe_2$ in this work. First-principles theory calculations show that 3*d* states of Fe transition element participate in valence band transportation, the effective mass increases from ~$2.21m_0$ in Fe-free sample to ~3.01 m_0 in $Ge_{0.9}Sb_{0.1}Te-2\%FeTe_2$ through enlarging density of state (DOS), leading to a high power factor. Additionally, we find that Van der Waals gaps and Fe-rich nanoprecipitates incorporate into the matrix by introducing $FeTe_2$, which significantly descends the lattice thermal conductivity to ~0.54 $Wm^{-1}K^{-1}$. Meanwhile, the defects and nanoscale second phases have a negligible effect on carrier mobility, which is devoted to a significant enhancement in quality factor *B*. Combining these advanced strategies, a maximum *ZT* of ~2.1 and a ZT_{ave} of ~1.25 over 303–773 K are acquired in $Ge_{0.9}Sb_{0.1}Te-1\%FeTe_2$. Our work confirms that superior TE performance can be achieved in GeTe-based materials with synergistically manipulating band structures and microstructures.

2. Results and discussion

Fig. 1 depicts the phase constitution identification of $Ge_{0.9}Sb_{0.1}Te$-*x*%$FeTe_2$ (x = 0, 0.5, 1.0, 1.5 and 2.0). As illustrated in Fig. 1(a), the power-XRD patterns of samples are well-matched with peaks of rhombohedral-GeTe (*R*3*m*) with no impurity phases. In particular, the double peaks 2θ ranging in 25–27° and 42–44°, a feature of rhombohedral structure in GeTe, show a tendency to merge, respectively. This trend demonstrates an increase in structural symmetry of samples compared to the pristine rhombohedral-GeTe. In other words, rhombohedral and cubic phases coexist in GeTe-based samples, which also has been well investigated in previous researches [16,41]. The lattice parameter along with *a* axis changes slightly with increasing amount of $FeTe_2$ as displayed in Fig. 1(b).

Density functional theory (DFT) is performed to gain a deep insight into how the band structure is modified by introducing $FeTe_2$ in GeTe. The band structures of $Ge_{26}FeTe_{27}$ and $Ge_{27}Te_{27}$ in low-temperature rhombohedral phases are calculated as shown in Fig. 2. Fe is a transition metal element with occupied 3*d*-state electronic orbitals. Arising from Fe 3*d* states, extra states are introduced in band gap by introducing $FeTe_2$, as illustrated in red dots in Fig. 2(a). The band calculations show that near the Fermi level of valence bands are composed mainly of Fe 3*d* states. In addition, DOS near the top of the valence band in intrinsic GeTe and $FeTe_2$-contained GeTe is displayed in Fig. 2(b). It can be seen that band gap descends after adding $FeTe_2$. The DOS plots present the obvious peaks near the Fermi level (E_F) in $FeTe_2$-introduced GeTe which are absent in pristine GeTe. Therefore, it can be concluded that introducing $FeTe_2$ has a significant effect on band structure and increases the density of states.

The specific impact of introducing $FeTe_2$ on electrical transport properties of $Ge_{0.9}Sb_{0.1}Te$-*x*%$FeTe_2$ (x = 0, 0.5, 1.0, 1.5 and 2.0) are illustrated in Fig. 3. The ambient temperature electrical conductivity enhances from 725 S cm^{-1} for the Fe-free sample to 955 S cm^{-1} for $Ge_{0.9}Sb_{0.1}Te-2\%FeTe_2$, as illustrated in Fig. 3(a). And the overall electrical conductivity (σ) increases with raising the amount of $FeTe_2$. Conversely, Fig. 3(b) displays that the overall Seebeck coefficient (S) reduces with raising $FeTe_2$ fraction. The Hall measurement presents an enhancement of carrier concentration in $Ge_{0.9}Sb_{0.1}Te-FeTe_2$ system with $FeTe_2$ content rising, from ~1.76 × 10^{20} cm^{-3} in $FeTe_2$-free sample to ~3.37 × 10^{20} cm^{-3} in $Ge_{0.9}Sb_{0.1}Te-2\%FeTe_2$ in Fig. 3(d). We speculate that introducing $FeTe_2$ may lead to the increment in carrier concentration through introducing extra Ge vacancy. To investigate the effect of the altered band structure on the carrier transport, we present Pisarenko relationship based on a single parabolic band (SPB) model and an assumption of acoustic phonon scattering in Fig. 3(c). The density of state (DOS) effective masses (m^*) of $Ge_{0.9}Sb_{0.1}Te$-*x*%$FeTe_2$ in this work are superior than those of other M-introduced (M = PbTe [42], GeSe [31], ZnTe [14], CdTe [17]) GeTe systems. The effective masses gradually enhance with the increase of carrier concentration, from ~$2.21m_0$ in Fe-free sample to ~$3.01m_0$ in $Ge_{0.9}Sb_{0.1}Te-2\%FeTe_2$ in Fig. 3(d), which results from the peaks near Fermi level (E_F) after introducing $FeTe_2$. The results are consistent with the DFT calculations mentioned above. Correspondingly, carrier mobility as a function of carrier concentration slightly decreases as illustrated in Fig. 3(e), which is rather high compared with other GeTe-based materials [29,31,43]. Although the DOS increases as discussed above, a decreased Seebeck coefficient as rising $FeTe_2$ fraction is obtained, resulting from the sharply increased carrier concentration. Combining the elevated σ and the slightly descended S, the

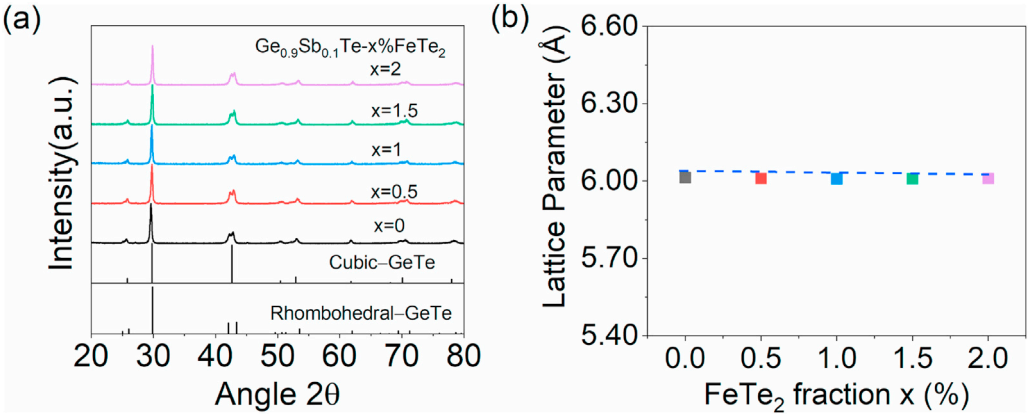

Fig. 1. Phase identification of $Ge_{0.9}Sb_{0.1}Te$-*x*%$FeTe_2$ (x = 0, 0.5, 1.0, 1.5 and 2.0): (a) powder XRD patterns and (b) lattice parameter along with a axis.

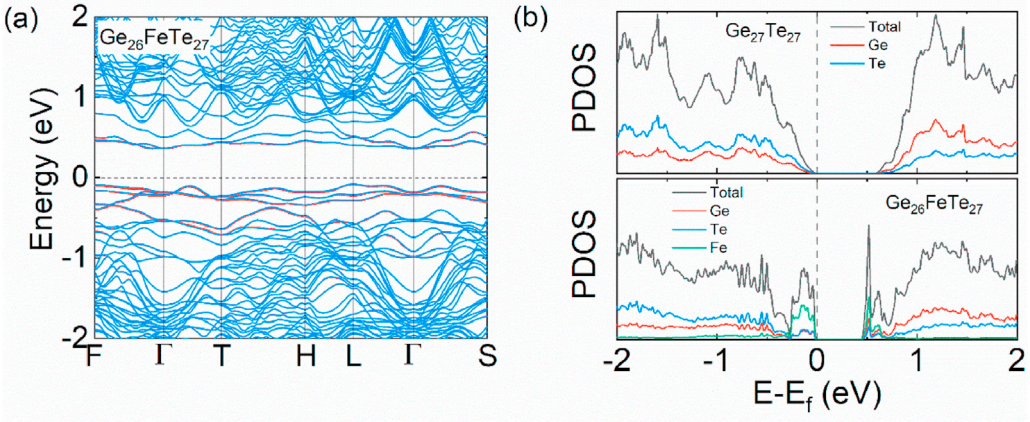

Fig. 2. (a) Band structures of $Ge_{26}FeTe_{27}$ and (b) density of states (DOS) of $Ge_{27}Te_{27}$ and $Ge_{26}FeTe_{27}$ in low-temperature rhombohedral structure.

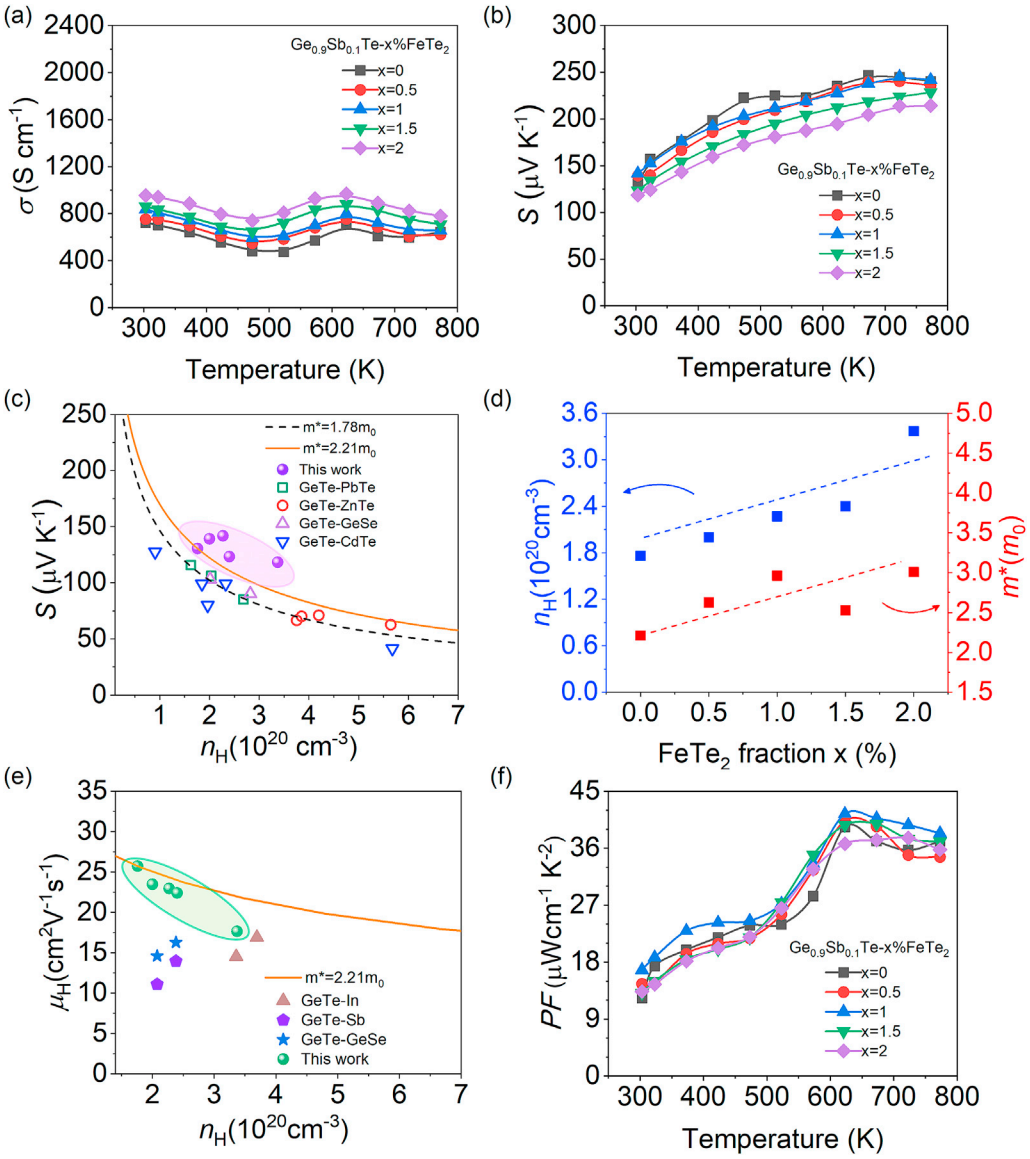

Fig. 3. Electrical transport properties of $Ge_{0.9}Sb_{0.1}Te$-x%$FeTe_2$ (x = 0, 0.5, 1.0, 1.5 and 2.0): (a) electrical conductivity; (b) Seebeck coefficient; (c) Pisarenko plot compared with previous results [14,17,31,42]; (d) ambient temperature carrier concentration and effective mass as a function of $FeTe_2$ content; (e) comparison of ambient temperature carrier mobility in $Ge_{0.9}Sb_{0.1}Te$-x%$FeTe_2$, GeTe-In [29], GeTe-Sb [43], GeTe-GeSe [31], and (f) power factor.

power factor (*PF*) is well maintained in $Ge_{0.9}Sb_{0.1}Te$-*x*%$FeTe_2$ ($x = 0$, 0.5, 1.0, 1.5 and 2.0), as depicted in Fig. 3(f). The peak power factor ~41 μWcm^{-1} K^{-2}at 623 K in $Ge_{0.9}Sb_{0.1}Te-1\%FeTe_2$ is achieved.

The thermal transport properties of $Ge_{0.9}Sb_{0.1}Te$-*x*%$FeTe_2$ ($x = 0$, 0.5, 1.0, 1.5 and 2.0) are illustrated in Fig. 4. The electronic thermal conductivities (κ_{ele}) are calculated using a Wiedemann–Franz relationship as depicted in Fig. 4(a). Due to the incremental carrier concentration, electronic thermal conductivities enhance with increasing $FeTe_2$ content. The lattice thermal conductivity (κ_{lat}) is attained by subtracting the κ_{ele} from the total thermal conductivity (κ_{tot}) as shown in Fig. 4(b). With rising $FeTe_2$ fraction, the overall κ_{lat} sharply decreases and slightly fluctuates at 573 K, coinciding with phase transition, which is verified by DSC measurement in Fig. S1. As displayed in the inset of Fig. 4(b), the κ_{lat} at 773 K largely reduces from ~0.81 Wm^{-1} K^{-1} in $FeTe_2$-free $Ge_{0.9}Sb_{0.1}Te$ to ~0.54 Wm^{-1} K^{-1} in $Ge_{0.9}Sb_{0.1}Te-2\%FeTe_2$. The attained minimum κ_{lat} in this work is ~33% reduction compared with that of $FeTe_2$-free $Ge_{0.9}Sb_{0.1}Te$, which approaches the κ_{min} on the base of the Cahill model [44]. Then, we compared the κ_{lat} of $Ge_{0.9}Sb_{0.1}Te-2\%FeTe_2$ to that of other high-*ZT* GeTe systems, such as GeTe-MnTe [32], GeTe-PbTe [42], GeTe-CdTe [17], GeTe-CrTe [45], GeTe-SiC [38], GeTe-SnSe-SnS [36]. It is worth noting that the present κ_{lat} of $Ge_{0.9}Sb_{0.1}Te-2\%FeTe_2$ is rather lower compared with others as illustrated in Fig. 4(c). Combing the effects between κ_{lat} and κ_{ele}, the total thermal conductivity initially descends with rising $FeTe_2$ content and then starts to increase in $Ge_{0.9}Sb_{0.1}Te$-1.5%$FeTe_2$ and $Ge_{0.9}Sb_{0.1}Te-2\%FeTe_2$. The overall total thermal conductivity descends with increasing temperature and then starts to enhance at 573 K. And other experimental data are illustrated in Fig. S2, including thermal diffusivity and Lorenz number.

To get an insight into the low lattice thermal conductivity, transmission electron microscopy (TEM) is performed to delve into the microstructures of $FeTe_2$-contained $Ge_{0.9}Sb_{0.1}Te$. As schemed in Fig. 5(a), we observed numerous ferroelectric domain structures with nanoscale in $Ge_{0.9}Sb_{0.1}Te-2\%FeTe_2$, which is a characteristic microstructure in the GeTe system [21,35,46]. Fig. 5(b) displays the enlarged image of the area marked in Fig. 5(a). Van der Waals gaps induced by Ge vacancy are discovered between alternating bright and dark stripes. And its corresponding selected area diffraction (SAED) pattern is indexed to the rhombohedral structure ($R3m$) along the zone axis of [010], as schemed in Fig. 5(c). However, the pattern of the matrix along [001] in other areas is identified to be cubic-GeTe ($Fm\bar{3}m$) as shown in Fig. S3, indicating that cubic and rhombohedral phases both exist in $Ge_{0.9}Sb_{0.1}Te-2\%FeTe_2$, which is consistent with our XRD data. Further, the TEM image of $Ge_{0.9}Sb_{0.1}Te-2\%FeTe_2$ in some areas shows the appearance of several second phases with irregular shapes as displayed in Fig. 5(d). The nanoprecipitates vary in size from 50 to 100 nm with random distribution in the samples. And the SAED pattern along [001] from regions with precipitates is illustrated in the inset of Fig. 5(g). Although STEM-energy dispersive X-ray spectroscopy (EDS) elemental maps of the precipitates reveal that they are Fe-rich phases as schemed in Fig. 5(f), the SAED patterns do not match with the patterns of either $FeTe_2$ or Fe-rich phases. However, it is worth noting that Fe-rich nanoprecipitates can strongly scatter phonons rather than carriers, which have a weak impact on carrier transport and maintain high carrier mobility. It is mainly because the size of nanoprecipitates much larger than the mean free path of carriers in GeTe [38,47]. Geometric phase analysis (GPA) is performed to explore the strain distribution around Fe-rich nanoprecipitates. Fig. 5(h) and (i) display GPA maps results acquired from Fig. 5(g). High ε_{xx} (horizontal axis) strain kernels exist at the

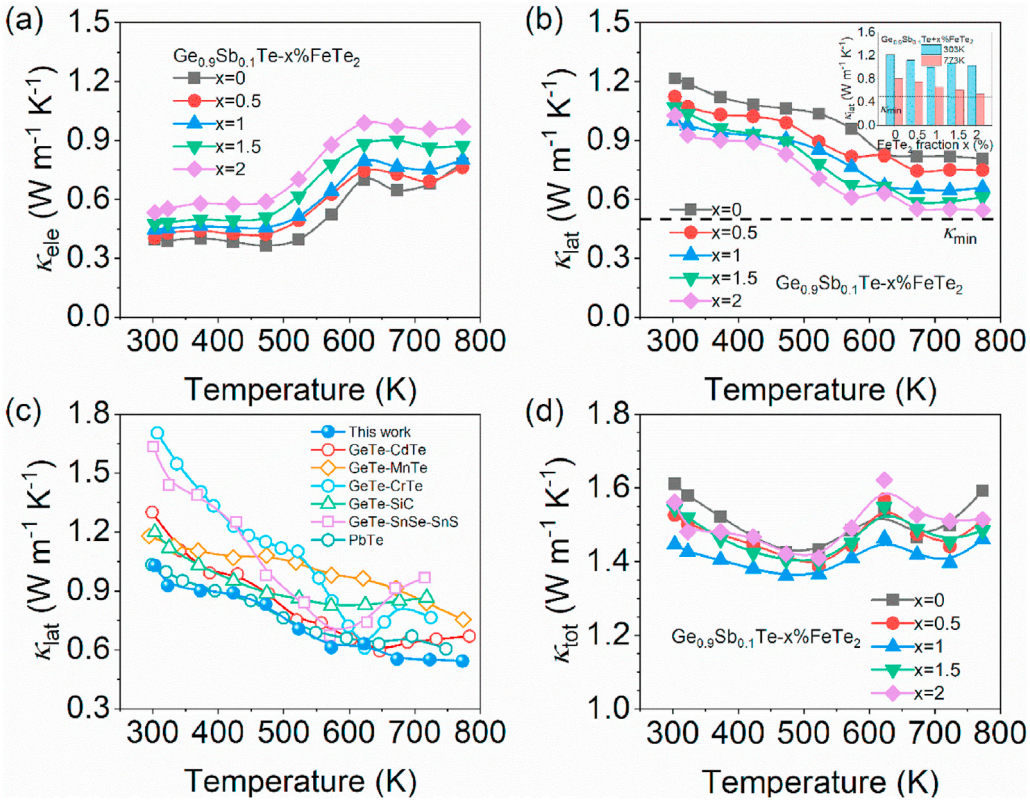

Fig. 4. Thermal transport properties of $Ge_{0.9}Sb_{0.1}Te$-*x*%$FeTe_2$ ($x = 0$, 0.5, 1.0, 1.5 and 2.0): (a) electronic thermal conductivity; (b) lattice thermal conductivity; (c) comparison of lattice thermal conductivity between $Ge_{0.9}Sb_{0.1}Te-FeTe_2$ and previous results [17,32,36,38,45], and (d) total thermal conductivity.

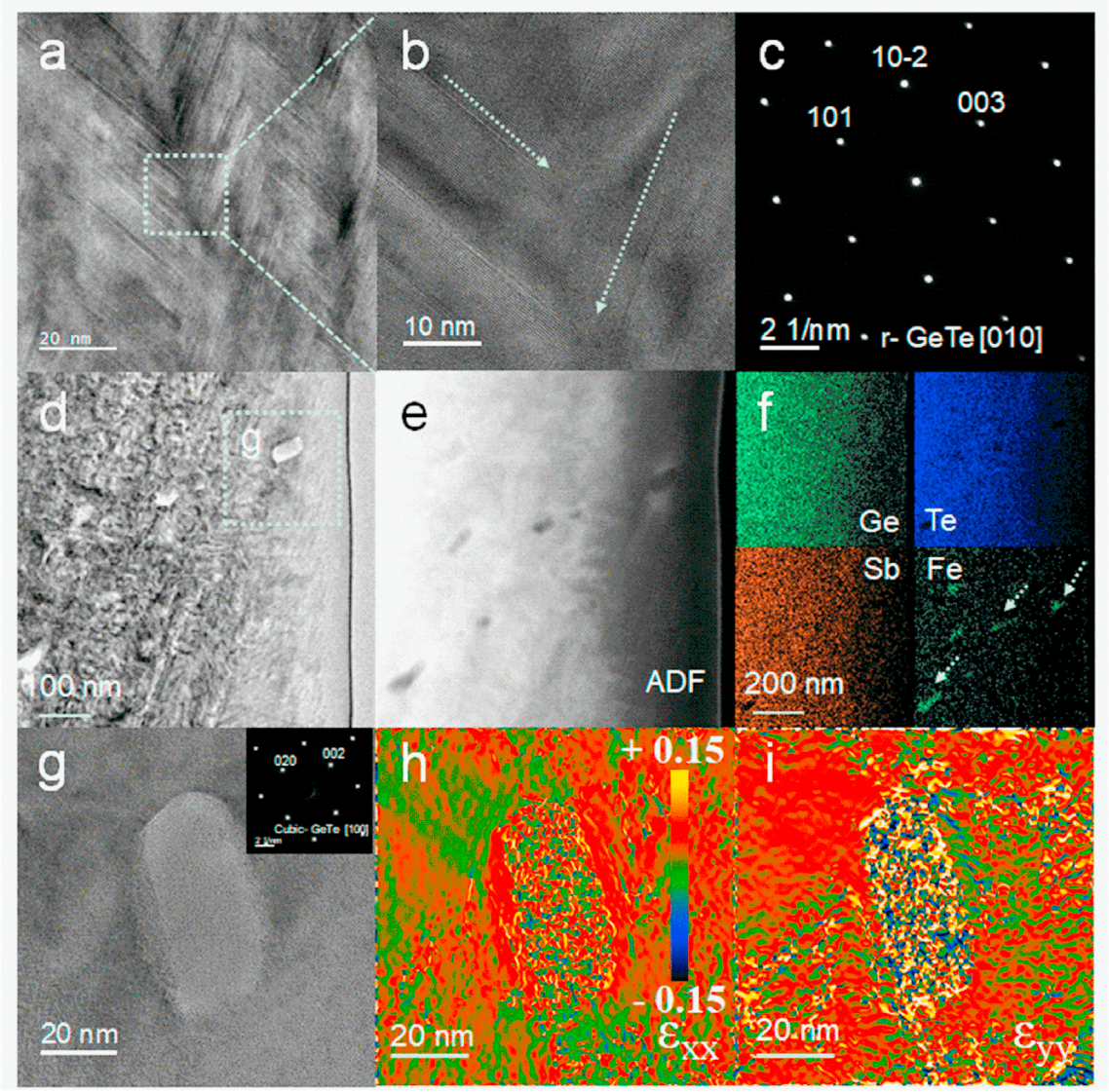

Fig. 5. (a) The low magnification TEM image of $Ge_{0.9}Sb_{0.1}Te-2\%FeTe_2$ showing typical ferroelectric domain structures of GeTe, (b) enlarge view of the region shown in (a) illustrating Van der Waals gaps, and (c) the SAED of the region showing rhombohedral structure GeTe along [010] axis. (d) The low magnification TEM image, (e) STEM ADF image, and (f) corresponding STEM-energy dispersive X-ray spectroscopy (EDS) elements distribution mapping of $Ge_{0.9}Sb_{0.1}Te-2\%FeTe_2$ sample showing several Fe-rich nanoprecipitates. (g) HRTEM image, the inset shows the SAED with cubic structure along [100], GPA strain analysis along (h) horizontal (ε_{xx}) and (i) vertical (ε_{yy}) directions of a rich-Fe nanoprecipitate of the framed area in (d).

boundary between the matrix and the precipitate, while high negative ε_{yy} (vertical axis) strain kernels appear at the midzone of the precipitate. All of these aforementioned, including Van der Waals gaps, nanoprecipitates and strain field fluctuations, significantly contribute to the intensification of phonon scattering.

The promoted TE properties can be well evaluated by the quality factor (B) with respect to interdependent TE parameters (effective mass m^*, lattice thermal conductivity κ_{lat}, and weighted carrier mobility μ_w). To thoroughly comprehend the role of $FeTe_2$ in $Ge_{0.9}Sb_{0.1}Te$, the quality factor B is estimated by the following equations [12,48].

$$\mu_W = \mu\left(\frac{m^*}{m_e}\right)^{3/2} \quad (1)$$

$$B = 9\frac{\mu_W}{\kappa_{lat}}\left(\frac{T}{300}\right)^{5/2} \quad (2)$$

where μ_w denotes weighted carrier mobility and T denotes absolute temperature. The calculation details of weighted carrier mobility are given in Support Information. As depicted in Fig. 6(a), the quality factor B undergoes a remarkable increment over the entire working temperature after introducing $FeTe_2$, especially in high temperature region. An enhancement of 28% in quality factor B is achieved in $Ge_{0.9}Sb_{0.1}Te-1\%FeTe_2$ at 623 K compared to that with $FeTe_2$-free sample, which derives from slightly decreased carrier mobility and largely suppressed κ_{lat}. By comparing the weighted carrier mobility and κ_{lat} of other GeTe-based materials at 623 K [17,29,32–34,38,43,49,50], it is found that $FeTe_2$-added $Ge_{0.9}Sb_{0.1}Te$ exhibits excellent thermoelectric properties through synergistically

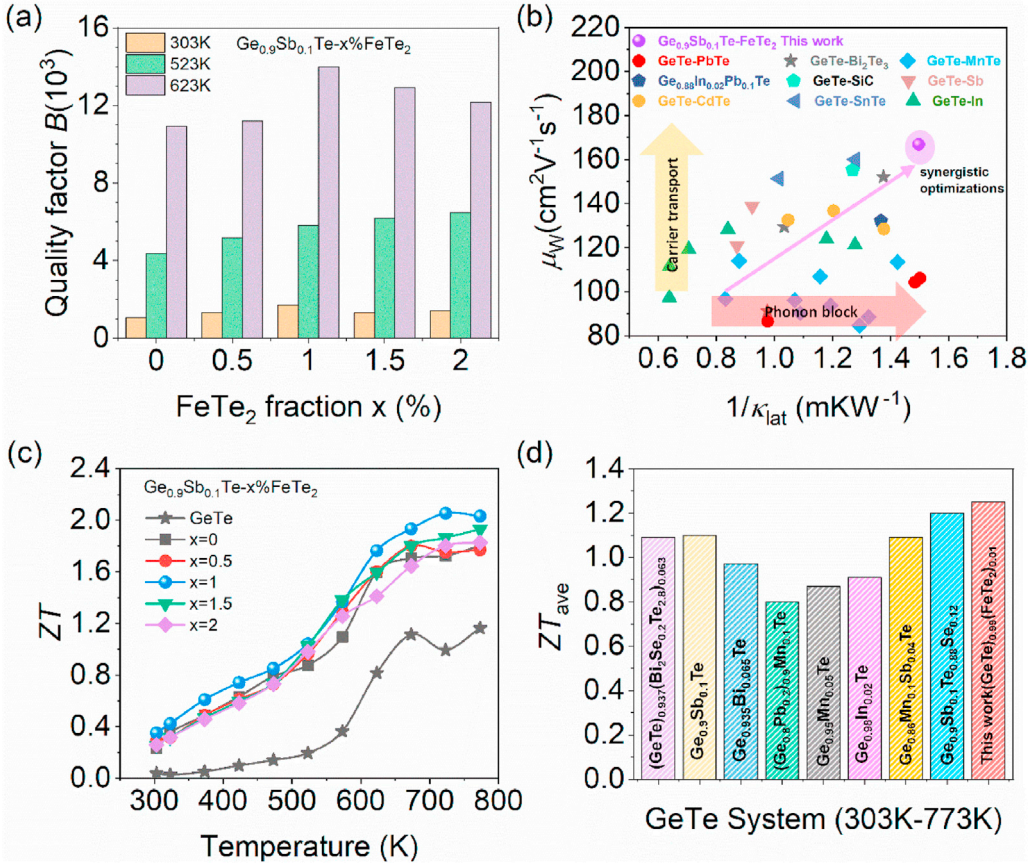

Fig. 6. Thermoelectric performance of $Ge_{0.9}Sb_{0.1}Te$-*x*%$FeTe_2$ ($x = 0$, 0.5, 1.0, 1.5 and 2.0): (a) calculated quality factor *B* as a function of $FeTe_2$ at 303 K, 523 K, and 623 K, respectively; (b) diagram of μ_w and $1/\kappa_{lat}$ compared with previous results (GeTe-PbTe [42], GeTe-Bi_2Te_3 [33], GeTe-MnTe [32], $Ge_{0.88}In_{0.02}Pb_{0.1}Te$ [34], GeTe-SiC [38], GeTe-Sb [43], GeTe-CdTe [17], GeTe-SnTe [50], and GeTe-In [29]); (c) *ZT* values; (d) comparison of ZT_{ave} between $Ge_{0.9}Sb_{0.1}Te$—$FeTe_2$ and previous reported datas (GeTe-$Bi_2Se_{0.2}Te_{2.8}$ [51], GeTe-Sb [43], GeTe-Bi [33], GeTe-Pb-Mn [52], GeTe-Mn [32], GeTe-In [29], GeTe-Sb-Mn [32], and GeTe-GeSe [31]).

promoting thermal and electrical transport properties, as schemed in Fig. 6(b).

Consequently, a peak *ZT* value ~2.1 and an average *ZT* of ~1.25 at 303—773 K are obtained in $Ge_{0.9}Sb_{0.1}Te$—1%$FeTe_2$ as illustrated in Fig. 6(c) and (d). The eminent thermoelectric performance in $FeTe_2$-introduced $Ge_{0.9}Sb_{0.1}Te$ is superior to that in other GeTe systems as illustrated in Fig. 6(d) and Fig. S4, such as ZT_{ave} ~1.09 in GeTe-$Bi_2Se_{0.2}Te_{2.8}$ [51], ZT_{ave} ~1.10 in GeTe-Sb [43], ZT_{ave} ~0.97 in GeTe-Bi [33], ZT_{ave} ~0.80 in GeTe-Pb-Mn [52], ZT_{ave} ~0.87 in GeTe-Mn [32], ZT_{ave} ~0.91 in GeTe-In [29], ZT_{ave} ~1.09 in GeTe-Sb-Mn [32], and ZT_{ave} ~1.20 in GeTe-GeSe [31]. This work proposes a direction for designing superior performance thermoelectric materials.

3. Conclusions

In summary, introducing $FeTe_2$ has a positive effect on thermoelectric performance of $Ge_{0.9}Sb_{0.1}Te$ through achieving high weighted carrier mobility and low lattice thermal conductivity. Compared with $FeTe_2$-free $Ge_{0.9}Sb_{0.1}Te$, the super electrical transport property can be well maintained through elevating the effective mass from ~$2.21m_0$ in Fe-free sample to ~$3.01m_0$ in $Ge_{0.9}Sb_{0.1}Te$—2%$FeTe_2$ *via* increasing density of states. Meanwhile, the lattice thermal conductivity can be dramatically suppressed through scattering phonon *via* Van der Waals gaps, Fe-rich nanoprecipitates and strain field fluctuations. Notably, a minimum lattice thermal conductivity reaches ~0.54 Wm^{-1} K^{-1} in $Ge_{0.9}Sb_{0.1}Te$—2%$FeTe_2$ at 773 K. Consequently, a remarkable elevation in quality factor *B* is attained in $FeTe_2$-introduced $Ge_{0.9}Sb_{0.1}Te$. A peak *ZT* ~2.1 is achieved in $Ge_{0.9}Sb_{0.1}Te$—1%$FeTe_2$ at 723 K, and its ZT_{ave} reaches ~1.25 in 303—773 K. This work opens prospects for optimizing TE performance by band structure and microstructure modulations.

Credit author statement

Yang Jin, Yuting Qiu and Li-Dong Zhao synthesized the samples, designed and carried out the experiments, analyzed the results and wrote the paper. Dongyang Wang carried out the DFT calculations. Yu Xiao and Wenke He carried out the Hall measurements. Tao Hong and Xiang Gao carried out the TEM experiments. All authors conceived the experiments, analyzed the results and co-edited the manuscript.

Declaration of competing interest

The authors declare that they have no known competing financial interests or personal relationships that could have appeared to influence the work reported in this paper.

Acknowledgments

This work was supported by National Natural Science Foundation of China (52002011 and 51772012), National Key Research and Development Program of China (2018YFA0702100 and 2018YFB0703600), the Beijing Natural Science Foundation (JQ18004), the Opening Project of State Key Laboratory of High

Performance Ceramics and Superfine Microstructure (SKL202005SIC), Shenzhen Peacock Plan team (KQTD20160226195659991) and 111 Project (B17002). This work was also supported by the National Postdoctoral Program for Innovative Talents (BX20200028). L.D.Z. appreciates the support of the high performance computing (HPC) resources at Beihang University, the National Science Fund for Distinguished Young Scholars (51925101), and center for High Pressure Science and Technology Advanced Research (HPSTAR) for SEM and TEM measurements.

Appendix A. Supplementary data

Supplementary data to this article can be found online at https://doi.org/10.1016/j.mtphys.2021.100444

References

[1] G.J. Snyder, E.S. Toberer, Nat. Mater. 7 (2008) 105–114.
[2] J.P. Heremans, V. Jovovic, E.S. Toberer, A. Saramat, K. Kurosaki, A. Charoenphakdee, S. Yamanaka, G.J. Snyder, Science 321 (2008) 554–557.
[3] Y. Pei, X. Shi, A. LaLonde, H. Wang, L. Chen, G.J. Snyder, Nature 473 (2011) 66–69.
[4] X. Qian, H. Wu, D. Wang, Y. Zhang, S.J. Pennycook, X. Gao, L. Zheng, L.D. Zhao, Mater. Today Phys. 9 (2019) 100102.
[5] Y. Zhou, H. Wu, D. Wang, L. Fu, Y. Zhang, J. He, S.J. Pennycook, L.D. Zhao, Mater. Today Phys. 7 (2018) 77–88.
[6] T. Zhu, Y. Liu, C. Fu, J.P. Heremans, J.G. Snyder, X. Zhao, Adv. Mater. 29 (2017) 1605884.
[7] C. Chang, L.-D. Zhao, Mater. Today Phys. 4 (2018) 50–57.
[8] H. Kang, Z. Yang, X. Yang, J. Li, W. He, Z. Chen, E. Guo, L.D. Zhao, T. Wang, Mater. Today Phys. 17 (2021) 100332.
[9] J. Dong, F.-H. Sun, H. Tang, J. Pei, H.-L. Zhuang, H.-H. Hu, B.-P. Zhang, Y. Pan, J.-F. Li, Energy Environ. Sci. 12 (2019) 1396–1403.
[10] S. Perumal, S. Roychowdhury, K. Biswas, Inorg. Chem. Front. 3 (2016) 125–132.
[11] K. Biswas, J. He, I.D. Blum, C.I. Wu, T.P. Hogan, D.N. Seidman, V.P. Dravid, M.G. Kanatzidis, Nature 489 (2012) 414–418.
[12] Y. Xiao, D.Y. Wang, Y. Zhang, C.R. Chen, S.X. Zhang, K.D. Wang, G.T. Wang, S.J. Pennycook, G.J. Snyder, H.J. Wu, L.D. Zhao, J. Am. Chem. Soc. 142 (2020) 4051–4060.
[13] W.H. Shin, J.W. Roh, B. Ryu, H.J. Chang, H.S. Kim, S. Lee, W.S. Seo, K. Ahn, ACS Appl. Mater. Interfaces 10 (2018) 3689–3698.
[14] M. Hong, Y. Wang, T. Feng, Q. Sun, S. Xu, S. Matsumura, S.T. Pantelides, J. Zou, Z.G. Chen, J. Am. Chem. Soc. 141 (2019) 1742–1748.
[15] G. Tan, F.Y. Shi, S.Q. Hao, H. Chi, L.D. Zhao, C. Uher, C. Wolverton, V.P. Dravid, M.G. Kanatzidis, J. Am. Chem. Soc. 137 (2015) 5100–5112.
[16] S. Perumal, P. Bellare, U.S. Shenoy, U.V. Waghmare, K. Biswas, Chem. Mater. 29 (2017) 10426–10435.
[17] M. Hong, Y. Wang, W. Liu, S. Matsumura, H. Wang, J. Zou, Z.-G. Chen, Adv. Energy Mater. 8 (2018) 1801837.
[18] D.T. Morelli, J.P. Heremans, C.M. Thrush, Phys. Rev. B 67 (2003): 035206.
[19] H. Mun, K.H. Lee, S.J. Kim, J.Y. Kim, J.H. Lee, J.H. Lim, H.J. Park, J.W. Roh, S.W. Kim, Materials 8 (2015) 959–965.
[20] J.P. Heremans, B. Wiendlocha, A.M. Chamoire, Energy Environ. Sci. 5 (2012) 5510–5530.
[21] D. Wu, L. Xie, X. Xu, J. He, Adv. Funct. Mater. 29 (2019) 1806613.
[22] L.D. Zhao, H.J. Wu, S.Q. Hao, C.I. Wu, X.Y. Zhou, K. Biswas, J.Q. He, T.P. Hogan, C. Uher, C. Wolverton, V.P. Dravid, M.G. Kanatzidis, Energy Environ. Sci. 6 (2013) 3346–3355.
[23] M. Samanta, S. Roychowdhury, J. Ghatak, S. Perumal, K. Biswas, Chem. Eur J. 23 (2017) 7438–7443.
[24] B. Poudel, Q. Hao, Y. Ma, Y. Lan, A. Minnich, B. Yu, X. Yan, D. Wang, A. Muto, D. Vashaee, X. Chen, J. Liu, M.S. Dresselhaus, G. Chen, Z. Ren, Science 320 (2008) 634–638.
[25] K. Biswas, J. He, Q. Zhang, G. Wang, C. Uher, V.P. Dravid, M.G. Kanatzidis, Nat. Chem. 3 (2011) 160–166.
[26] M.G. Kanatzidis, Chem. Mater. 22 (2010) 648–659.
[27] G.J. Tan, L.D. Zhao, F.Y. Shi, J.W. Doak, S.H. Lo, H. Sun, C. Wolverton, V.P. Dravid, C. Uher, M.G. Kanatzidis, J. Am. Chem. Soc. 136 (2014) 7006–7017.
[28] M. Hong, J. Zou, Z.G. Chen, Adv. Mater. 31 (2019): e1807071.
[29] L. Wu, X. Li, S. Wang, T. Zhang, J. Yang, W. Zhang, L. Chen, J. Yang, NPG Asia Mater. 9 (2017) e343.
[30] R.K. Vankayala, T.W. Lan, P. Parajuli, F. Liu, R. Rao, S.H. Yu, T.L. Hung, C.H. Lee, S.i. Yano, C.R. Hsing, D.L. Nguyen, C.L. Chen, S. Bhattacharya, K.H. Chen, M.N. Ou, O. Rancu, A.M. Rao, Y.Y. Chen, Adv. Sci. (2020) 2002494.
[31] J. Li, X. Zhang, S. Lin, Z. Chen, Y. Pei, Chem. Mater. 29 (2016) 605–611.
[32] Z. Zheng, X. Su, R. Deng, C. Stoumpos, H. Xie, W. Liu, Y. Yan, S. Hao, C. Uher, C. Wolverton, M.G. Kanatzidis, X. Tang, J. Am. Chem. Soc. 140 (2018) 2673–2686.
[33] Y. Jin, Y. Xiao, D. Wang, Z. Huang, Y. Qiu, L.-D. Zhao, ACS Appl. Energy Mater. 2 (2019) 7594–7601.
[34] Y. Qiu, Y. Jin, D. Wang, M. Guan, W. He, S. Peng, R. Liu, X. Gao, L.-D. Zhao, J. Mater. Chem. A 7 (2019) 26393–26401.
[35] X. Xu, L. Xie, Q. Lou, D. Wu, J. He, Adv. Sci. 5 (2018) 1801514.
[36] P. Acharyya, S. Roychowdhury, M. Samanta, K. Biswas, J. Am. Chem. Soc. 142 (2020) 20502–20508.
[37] M. Samanta, K. Biswas, J. Am. Chem. Soc. 139 (2017) 9382–9391.
[38] Y. Jin, X. Zhang, Y. Xiao, W. He, D. Wang, J. Li, S. Zheng, D. Ren, Y. Qiu, L.-D. Zhao, Scripta Mater. 183 (2020) 22–27.
[39] Y. Jin, D. Wang, Y. Qiu, L.-D. Zhao, J. Mater. Chem. C 9 (2021) 6484–6490.
[40] J.C. Grivel, A.C. Wulff, Y. Zhao, J. Bednarčík, M.v. Zimmermann, J. Mater. Sci. 46 (2011) 4540–4544.
[41] Y.F. Tsai, P.C. Wei, L. Chang, K.K. Wang, C.C. Yang, Y.C. Lai, C.R. Hsing, C.M. Wei, J. He, G.J. Snyder, H.J. Wu, Adv. Mater. 33 (2020): e2005612.
[42] X. Zhang, J. Li, X. Wang, Z. Chen, J. Mao, Y. Chen, Y. Pei, J. Am. Chem. Soc. 140 (2018) 15883–15888.
[43] S. Perumal, S. Roychowdhury, D.S. Negi, R. Datta, K. Biswas, Chem. Mater. 27 (2015) 7171–7178.
[44] D.G. Cahill, S.K. Watson, R.O. Pohl, Phys. Rev. B 46 (1992) 6131–6140.
[45] J. Shuai, Y. Sun, X. Tan, T. Mori, Small 16 (2020): e1906921.
[46] L. Xie, Y. Chen, R. Liu, E. Song, T. Xing, T. Deng, Q. Song, J. Liu, R. Zheng, X. Gao, S. Bai, L. Chen, Nanomater. Energy 68 (2020) 104347.
[47] T. Zhu, H. Gao, Y. Chen, X. Zhao, J. Mater. Chem. A 2 (2014) 3251–3256.
[48] G. Tan, L.D. Zhao, M.G. Kanatzidis, Chem. Rev. 116 (2016) 12123–12149.
[49] J. Li, X. Zhang, X. Wang, Z. Bu, L. Zheng, B. Zhou, F. Xiong, Y. Chen, Y. Pei, J. Am. Chem. Soc. 140 (2018) 16190–16197.
[50] M. Hong, W. Lyv, M. Li, S. Xu, Q. Sun, J. Zou, Z.-G. Chen, Joule 4 (2020) 2030–2043.
[51] J. Koenig, M. Winkler, T. Dankwort, A.L. Hansen, H.F. Pernau, V. Duppel, M. Jaegle, K. Bartholome, L. Kienle, W. Bensch, Dalton Trans. 44 (2015) 2835–2843.
[52] Z.W. Lu, J.Q. Li, C.Y. Wang, Y. Li, F.S. Liu, W.Q. Ao, J. Alloys Compd. 621 (2015) 345–350.